# LETTER

# Past extreme warming events linked to massive carbon release from thawing permafrost

Robert M. DeConto[1], Simone Galeotti[2], Mark Pagani[3], David Tracy[1], Kevin Schaefer[4], Tingjun Zhang[4,7], David Pollard[5] & David J. Beerling[6]

Between about 55.5 and 52 million years ago, Earth experienced a series of sudden and extreme global warming events (hyperthermals) superimposed on a long-term warming trend[1]. The first and largest of these events, the Palaeocene–Eocene Thermal Maximum (PETM), is characterized by a massive input of carbon, ocean acidification[2] and an increase in global temperature of about 5 °C within a few thousand years[3]. Although various explanations for the PETM have been proposed[4–6], a satisfactory model that accounts for the source, magnitude and timing of carbon release at the PETM and successive hyperthermals remains elusive. Here we use a new astronomically calibrated cyclostratigraphic record from central Italy[7] to show that the Early Eocene hyperthermals occurred during orbits with a combination of high eccentricity and high obliquity. Corresponding climate–ecosystem–soil simulations accounting for rising concentrations of background greenhouse gases[8] and orbital forcing show that the magnitude and timing of the PETM and subsequent hyperthermals can be explained by the orbitally triggered decomposition of soil organic carbon in circum-Arctic and Antarctic terrestrial permafrost. This massive carbon reservoir had the potential to repeatedly release thousands of petagrams ($10^{15}$ grams) of carbon to the atmosphere–ocean system, once a long-term warming threshold had been reached just before the PETM. Replenishment of permafrost soil carbon stocks following peak warming probably contributed to the rapid recovery from each event[9], while providing a sensitive carbon reservoir for the next hyperthermal[10]. As background temperatures continued to rise following the PETM, the areal extent of permafrost steadily declined, resulting in an incrementally smaller available carbon pool and smaller hyperthermals at each successive orbital forcing maximum. A mechanism linking Earth's orbital properties with release of soil carbon from permafrost provides a unifying model accounting for the salient features of the hyperthermals.

The PETM is characterized by a shift of >3‰ in the stable carbon isotopic composition ($\delta^{13}C$) of the surficial carbon pool, implying a huge injection of $^{13}C$-depleted carbon into the ocean and atmosphere. The source of this carbon is commonly attributed to the release of $^{13}C$-depleted methane from the destabilization of marine methane clathrates[6]. The isotopic composition of this source ($\delta^{13}C = -60‰$) provides a reasonable explanation for the isotope shift, but implies a carbon release (of ~2,000 Pg C) that is both inadequate to explain the magnitude of observed warming[11,12] and difficult to justify in clathrate modelling studies[13]. Other proposed carbon sources include a comet impact[14], a global conflagration of peat deposits[5], thermogenic $CO_2$ and $CH_4$ production in the North Atlantic[15], and the desiccation of organic matter in shallow continental seaways[4]. However, these suppositions fail to explain the sequence of multiple, progressively smaller hyperthermals that occurred over a three-million-year interval following the PETM[1,16]. The possibility that these events correspond to similar orbital geometries[17] suggests they share a common trigger mechanism and are not driven by rare events, tectonics or stochastic processes.

We investigated the relationship between orbital forcing and the timing of hyperthermals by determining their astrochronological age in the Contessa Road outcrop near Gubbio, Italy (Fig. 1 and Supplementary Information). The evolutive spectrum (obtained using wavelet analysis) of mean summer insolation at 75 °S[18] shows maxima at irregular intervals resulting from the combination of the long-term modulation of orbital eccentricity (2.4 Myr) and obliquity (1.2 Myr). Peaks in high-latitude insolation at concomitant maxima in the long (405-kyr) eccentricity and (1.2-Myr) obliquity bands in Cenozoic astronomical solutions[18] correspond with the onset of the major hyperthermal events at ~55.7 Myr ago (the PETM, also known as Eocene Thermal Maximum 1, ETM1), ~53.7 Myr ago (ETM2) ~52.4 Myr ago (ETM3), and other smaller events recorded in different settings[16,19]. Uncertainties in orbital solutions older than ~40 Myr (ref. 18) preclude the unequivocal orbital tuning of specific Eocene events. However, the floating cyclochronology at Contessa Road allows long-term modulation patterns to be determined, regardless of absolute ages. In our analysis, PETM (ETM1), ETM2 and ETM3 all align with obliquity and eccentricity maxima irrespective of which absolute age model is used[7,19]. This coincidence of hyperthermals with combined high-eccentricity and high-obliquity forcing points to the influence of polar latitudes, where seasonal insolation is strongly affected by obliquity and precession during high-eccentricity orbits.

We propose that the hyperthermals are linked to high-latitude orbital forcing through carbon-cycle feedbacks involving permafrost soil carbon (PFSC). The soil carbon reservoir has been dismissed as too small to cause an event like the PETM[4], but this view overlooks the potential for large PFSC stocks on Antarctica, before the continent became glaciated around 34 Myr ago. Carbon is frozen into permafrost through aeolian deposition, alluvial sedimentation and vertical peat deposition, which slowly increase soil depth on timescales of decades to millennia[20]. As sedimentation increases soil depth, roots and organic material at the bottom of the active layer become frozen into the permafrost, sequestering this organic matter from the active carbon cycle. A new reconstruction of Antarctic palaeogeography[21] shows that West Antarctica was mostly subaerial during the Palaeogene, increasing the continent's surface area by ~25% relative to today. Assuming that Antarctica remained mostly ice-free through the late Palaeocene and early Eocene, most of its $12.1 \times 10^6$ km$^2$ land surface would have been covered by forest and tundra (Fig. 2a), with the potential for storing massive amounts of permafrost carbon. Moreover, the continent's polar position would have made these frozen carbon stocks sensitive to the high-obliquity and high-eccentricity orbital forcing corresponding to the onset of the hyperthermals.

We tested the sensitivity of polar ecosystems and permafrost to increasing greenhouse-gas (GHG) concentrations[8], high-obliquity

[1]Department of Geosciences, University of Massachusetts, Amherst, Massachusetts 01002, USA. [2]Earth, Life, and Environmental Sciences Department, University of Urbino, 61029 Urbino, Italy. [3]Department of Geology and Geophysics, Yale University, New Haven, Connecticut 06520, USA. [4]National Snow and Ice Data Center, Cooperative Institute for Research in Environmental Sciences, University of Colorado at Boulder, Boulder, Colorado 80309, USA. [5]Earth and Environmental Systems Institute, Pennsylvania State University, University Park, Pennsylvania 16802, USA. [6]Department of Animal and Plant Sciences, University of Sheffield, Sheffield S10 2TN, UK. [7]Ministry of Education Key Laboratory of West China's Environmental System, Lanzhou University, 222 Tianshuinanlu, Lanzhou, Gansu 730000, China.
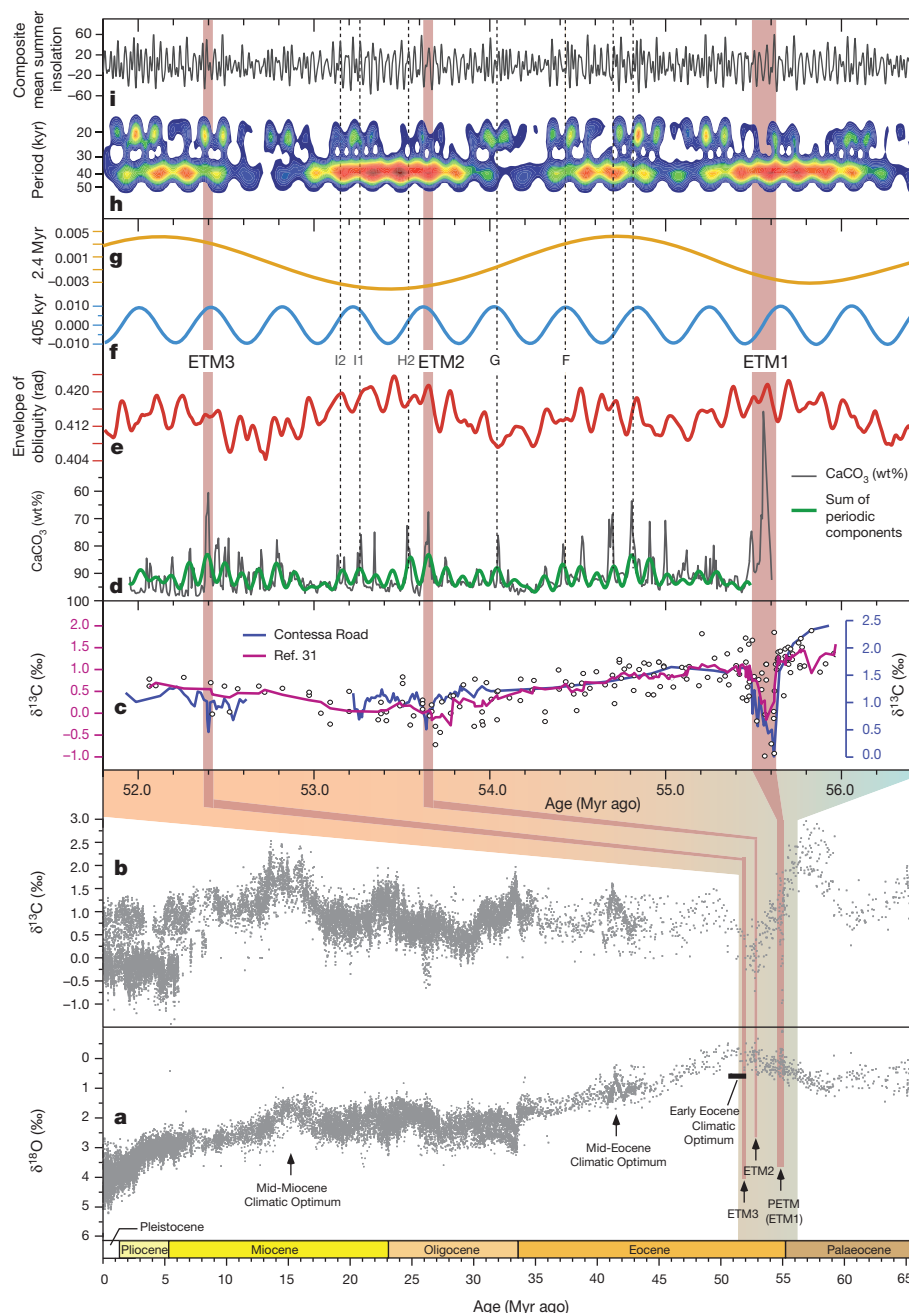
**Figure 1 | Orbital phasing of Early Eocene hyperthermals. a, b,** The Cenozoic record of benthic oxygen (**a**) and carbon (**b**) isotope values[31] shows the late Palaeocene–early Eocene gradual warming trend (shaded blue to red) that culminates at the Early Eocene Climatic Optimum. Positions of hyperthermals PETM (ETM1), ETM2 and ETM3 are shown. Panels above show the shaded area in more detail. **c,** Major early Eocene hyperthermals recorded in the bulk carbon isotope record from Contessa Road (blue line) relative to the benthic carbon isotope stack in ref. 31 (dots and pink line). **d,** $CaCO_3$ record from the Contessa Road section (grey line) and MTM reconstruction of individual components exceeding the 99% confidence level (green line). **e,** Envelope (Hilbert transform) of the obliquity parameter from the La04 astronomical solution[18]. **f,** The long-term (405 kyr) modulation component of eccentricity from La04[18]. **g,** The very long-term (~2.4 Myr)

modulation component of eccentricity from La04[18]. The astrochronological age of PETM (ETM1), ETM2 and ETM3 (grey bands) is based on Contessa Road. The inferred positions of other minor dissolution events and carbon isotope excursions (CIE; dashed lines), including F, G, H2, I1, I2 and the two unnamed events between 54.6 and 54.8 Myr ago[16,17,19], are also shown. All major events (ETMs) occur at maximum values of obliquity and minimal $CaCO_3$ values, and mimic the long-term modulation of obliquity. **h,** Evolutive spectrum of composite mean summer insolation (CMSI) at high latitudes shows intervals of maximum power in the higher frequency components (precession and obliquity) across hyperthermals. **i,** The CMSI series obtained by summing mean summer insolation at 65° N (21 June to 21 September) and 75° S (21 December to 21 March). The 65° N insolation values are doubled to account for the larger land area of the Northern Hemisphere (see Supplementary Information).

and high-eccentricity orbital forcing, and underlying long-term warming between ~62 and 52 Myr ago (Fig. 1) using a Global Climate Model (GCM) with coupled terrestrial biosphere and soil components (Methods). The simulations (Table 1) account for Early Eocene palaeogeography (Supplementary Information) with a larger, ice-free Antarctica[21] and progressively increasing $CO_2$, $CH_4$ and $N_2O$

atmospheric mixing ratios[8]. Four different prescribed orbits were applied at each GHG level (Table 1). The orbits include a mean orbital configuration with moderate obliquity and zero eccentricity (no precession forcing), a simulation with high obliquity and zero eccentricity, and two simulations with combined high obliquity and high eccentricity, corresponding to the onset of the hyperthermals (Fig. 1). In simulations
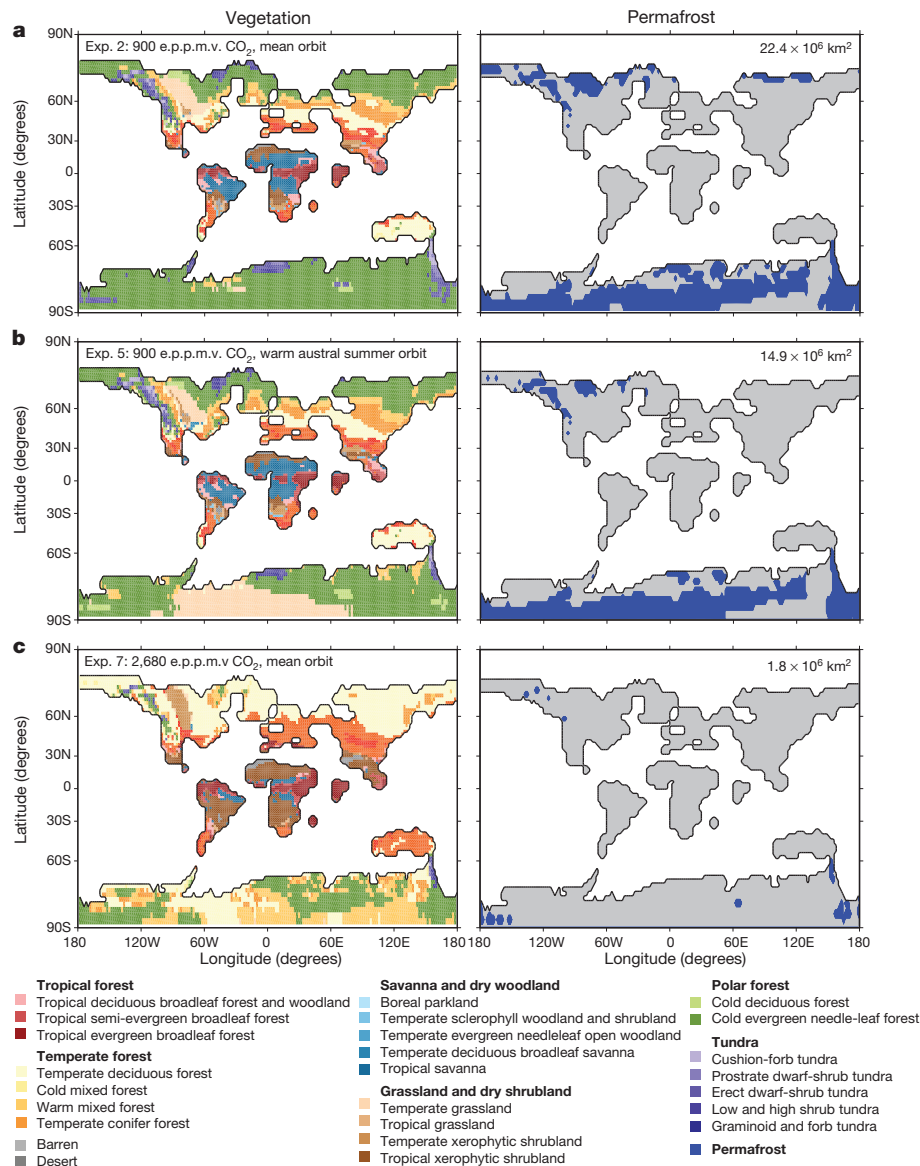
**Figure 2 | Climate-biome and permafrost simulations in response to increasing background GHG levels and orbital forcing.** Left, simulated biomes (corresponding vegetation types are shown below); right, permafrost (blue). $CO_2$ concentrations in equivalent parts per million by volume (e.p.p.m.v.) are shown at the top left of each panel and total permafrost area is shown at top right. Panels **a**–**c** represent a scenario of gradually increasing background GHG levels, leading to experiment 2 (Table 1) at 900 e.p.p.m.v. $CO_2$ (**a**), initial permafrost thaw and carbon release triggered by high-obliquity and high-eccentricity orbital forcing (**b**; corresponds to experiment 5 in Table 1), and enough carbon mobilized to increase GHG concentrations above 2,680 e.p.p.m.v. $CO_2$, causing 6 °C warming (**c**; corresponds to experiment 7 in Table 1).

**Table 1 | Climate-biome simulations, relevant inputs, and permafrost areas**

| Exp. | *$CO_2$ (e.p.p.m.v.) | $CO_2$ (p.p.m.v.) | $CH_4$ (p.p.b.v.) | $N_2O$ (p.p.b.v.) | Ecc. | Prec. (°) | Obl. (°) | MAT (°C) | NH PF ($10^6$ km$^2$) | SH PF ($10^6$ km$^2$) | Tot. PF ($10^6$ km$^2$) |
|---|---|---|---|---|---|---|---|---|---|---|---|
| Cont. | 400 | 355 | 1714 | 311 | 0.017 | 77.06 | 23.765 | 14.65 | 23.72 | NA | 23.72 |
| 1 | 550 | 500 | 1200 | 350 | 0.00 | 0.00 | 23.5 | 18.31 | 19.47 | 11.77 | 31.24 |
| **2** | **900** | **750** | **2100** | **375** | **0.00** | **0.00** | **23.5** | **20.30** | **12.04** | **10.31** | **22.35** |
| 3 | 900 | 750 | 2100 | 375 | 0.00 | 0.00 | 24.5 | 20.58 | 7.24 | 9.70 | 16.94 |
| 4 | 900 | 750 | 2100 | 375 | 0.05 | 270.00 | 24.5 | 20.63 | 5.82 | 9.70 | 15.52 |
| **5** | **900** | **750** | **2100** | **375** | **0.05** | **90.00** | **24.5** | **20.92** | **5.77** | **9.21** | **14.98** |
| 6 | 1,275 | 1,000 | 3000 | 400 | 0.00 | 0.00 | 23.5 | 22.39 | 1.59 | 8.27 | 9.86 |
| **7** | **2,680** | **2,000** | **3500** | **450** | **0.00** | **0.00** | **23.5** | **26.30** | **0.45** | **1.33** | **1.78** |
| 8 | 5,360 | 4,000 | 3500 | 450 | 0.00 | 0.00 | 23.5 | 30.45 | NA | NA | NA |

Experiments (Exp.) 2, 5 and 7 (bold font) correspond to the warming/orbital sequence in Fig. 2. *$CO_2$ is the equivalent volume mixing ratio (e.p.p.m.v.) of each simulation, if only $CO_2$ were increased and $CH_4$ and $N_2O$ were held at their pre-industrial levels of 700 and 270 p.p.b.v., respectively. Ecc., eccentricity. Prec., precession (the prograde angle from perihelion to the vernal equinox). Obl., obliquity (that is, tilt). Simulations with zero eccentricity and obliquity at 23.5° (exp. 1, 2, 6, 7, 8) correspond to the mean orbit simulations discussed in the text. MAT, simulated global-mean annual surface (2 m) air temperature. Permafrost (PF) areas in the Northern Hemisphere (NH) and the Southern Hemisphere (Antarctica; SH), and the total permafrost area (Tot.) are given. An equilibrated modern control simulation (Cont.) is shown for comparison with observations. Experiment 2 provides the pre-PETM baseline climate for our carbon calculations, as supported by terrestrial data-model comparisons (Supplementary Information). NA, not applicable.

with combined high eccentricity and high obliquity, precession is varied to place perihelion in either January or July, producing summers with high-intensity insolation over one pole and summers with lower insolation intensity but longer duration over the other.

Simulations with 550–900 effective parts per million by volume (e.p.p.m.v.) $CO_2$ (Table 1) representing pre-PETM (late Palaeocene) conditions show polar latitudes dominated by tundra, evergreen forest, and permafrost—environments well suited to sequestering PFSC[22] (Fig. 2a). At 900 e.p.p.m.v. $CO_2$, global-mean surface temperature is 6 °C warmer than today and Antarctic summers are too warm to allow glaciation; but $22.4 \times 10^6$ km$^2$ of permafrost (roughly equivalent to the total modern inventory) remains in the high latitudes of both hemispheres. The 900 e.p.p.m.v. $CO_2$ simulation (experiment 2) compares favourably with terrestrial estimates of late Palaeocene mean annual temperature (MAT) over a range of latitudes (Supplementary Information), indicating that it broadly represents late Palaeocene climate with substantial permafrost in the higher terrain of both poles.

In a framework of gradual warming, annual surface heat budgets in the permafrost zone approach net-zero as GHG levels reach 900 e.p.p.m.v. $CO_2$, making permafrost stability highly sensitive to orbital forcing once this threshold is reached. Relative to the simulation with a mean orbit (experiment 2), the combination of high obliquity and high eccentricity increases summer insolation by more than 85 W m$^{-2}$ over one pole, while increasing summer duration over the other (Supplementary Information). With high eccentricity, total permafrost area is most sensitive to a warm austral summer orbit (experiment 5), but both hemispheres lose permafrost simultaneously regardless of the timing of perihelion (Table 1), because permafrost is sensitive to both high-intensity and long-duration summers. At 900 e.p.p.m.v. $CO_2$, the combination of high-eccentricity and high-obliquity orbital forcing reduces the global permafrost region by $7.4 \times 10^6$ km$^2$ (33%). Simulations with high obliquity and zero eccentricity also show reductions in permafrost due to increased seasonality, but the combined effect of high obliquity and high eccentricity is greater (Table 1), with the potential to thaw vast areas of permafrost once a warming threshold is reached.

We estimate the response of the soil carbon reservoir to these orbitally driven changes in permafrost area by calculating the available PFSC reservoir in the areas that undergo thaw. Lacking details of Palaeocene–Eocene topography and observations of long-term permafrost depositional processes (especially in the Antarctic interior), we calculate the available PFSC in each simulation by assuming that past permafrost conditions were similar to today (Methods). A range of observed values of fractional wetland area, carbon density, and carbon deposit thickness in the permafrost zone are used to produce an ensemble of plausible PFSC inventories, providing a best estimate of the reservoir in each simulation and an estimate of uncertainty (Table 2). The PFSC reservoir in our modern control simulation (1,526 Pg C) is close to observations (1,672 Pg C)[22], but our Palaeogene values are probably underestimated, because they assume that the fraction of wetland, ancient carbon densities, and vertical accumulations in the permafrost zone are comparable to those in analogous modern settings. In contrast, Palaeocene–Eocene wetlands

are estimated to have been ~3 times more extensive than today[8,23,24], as supported by an analysis of the ancient topography (Supplementary Information), indicating a greater fractional land area capable of supporting peat formation. Furthermore, unlike the Quaternary, the polar regions of the early Cenozoic remained undisturbed by ice sheets for millions of years, with the potential for $>10^6$ years of continuous carbon deposition before the PETM and between major hyperthermals (Fig. 1). Hence, more extensive and thicker PFSC deposits than those considered here are probable, as evidenced by >10-m-thick Palaeogene coal deposits in some polar locations[25]. Such deposits could also account for trends in marine sulphur and carbon isotopes, indicating massive terrestrial carbon burial before the PETM[5]. Regardless, the conservative approach used here still points to a massive and vulnerable terrestrial carbon pool on a world free of major ice sheets.

Assuming that experiment 2 (Fig. 2a) broadly represents late Palaeocene climate, our best estimate of the pre-PETM PFSC carbon pool is $3,728 \pm 1,033$ Pg C (Table 2), nearly half of which is in Antarctica. This estimate more than doubles if we assume that the permafrost region in the wetter Palaeogene was dominated by peatland. After reaching a warming threshold at ~900 e.p.p.m.v. $CO_2$, the combination of high-eccentricity and high-obliquity orbital forcing releases more than 1,200 Pg C to the atmosphere. Perihelion during austral summer (experiment 5) causes the greatest carbon release ($1,237 \pm 331$ Pg C), although perihelion during boreal summer (experiment 4) has a nearly equivalent effect. This initial carbon input at rates up to ~1.5 Pg C yr$^{-1}$ has the potential to raise atmospheric $CO_2$ by more than 550 p.p.m.v. (see Methods), providing additional radiative forcing, more warming and further permafrost loss. As illustrated by the sequence of simulations in Fig. 2, this orbitally triggered permafrost–carbon–warming feedback liberates almost the entire global PFSC reservoir, releasing $3,434 \pm 951$ Pg C within the observed $10^4$-year timescale of carbon release. This raises global-mean temperature in our model by 6 °C (Table 1), accounting for the warming at the PETM (ETM1) without invoking high climate sensitivity to $CO_2$ or additional feedbacks involving other carbon reservoirs[6]. Furthermore, our estimates of carbon release from the PFSC reservoir are broadly consistent with geochemical model constraints[11,12] and provide an explanation for a previously unexplained pulse of organic carbon into the Southern Ocean at the PETM (ETM1)[26].

These results show the potential for high-latitude climate forcing to trigger massive terrestrial carbon release, initiating positive warming feedbacks that can account for the sudden and extreme nature of past hyperthermals. We find that Antarctica and high elevations of the circum-Arctic were suitable locations for massive carbon storage during the late Palaeocene and Early Eocene. During long-term warming, these environments eventually reached a climatic threshold, at which permafrost thaw and sudden release of stored soil carbon[27] were triggered during maxima in the long eccentricity and obliquity orbital cycles (Supplementary Fig. 1). This model calls on the direct release of $CO_2$ from the decomposition of terrestrial PFSC reserves, although background fluxes of $CH_4$ and $N_2O$ were probably enhanced[8,28], possibly contributing additional warming through atmospheric water vapour and cloud feedbacks[24]. Following the exhaustion of the PFSC

**Table 2 | Simulated permafrost soil carbon**

| Exp. | *$CO_2$ (e.p.p.m.v.) | NH PFSC (Pg C) | Antarctic PFSC (Pg C) | Global PFSC (Pg C) | Release (Pg C) |
|---|---|---|---|---|---|
| Cont. | 400 | 1526 | 0 | 1,526 | NA |
| 1 | 550 | $3,268 \pm 901$ | $1,976 \pm 545$ | $5,245 \pm 1,446$ | NA |
| **2** | **900** | **$2,008 \pm 557$** | **$1,720 \pm 477$** | **$3,728 \pm 1,033$** | **NA** |
| 3 | 900 | $962 \pm 269$ | $1,604 \pm 448$ | $2,800 \pm 782$ | $929 \pm 253$ |
| 4 | 900 | $964 \pm 267$ | $1,538 \pm 426$ | $2,591 \pm 717$ | $1,138 \pm 316$ |
| **5** | **900** | **$1,203 \pm 334$** | **$1,612 \pm 448$** | **$2,491 \pm 692$** | **$1,237 \pm 341$** |
| 6 | 1,275 | $264 \pm 73$ | $1,372 \pm 382$ | $1,636 \pm 455$ | $2,093 \pm 578$ |
| **7** | **2,680** | **$74 \pm 21$** | **$221 \pm 62$** | **$295 \pm 82$** | **$3,434 \pm 951$** |
| 8 | 5,360 | 0 | 0 | 0 | $3,728 \pm 1,033$ |

Northern Hemisphere (NH), Antarctic, and global total permafrost soil carbon (PFSC) in each simulation are ensemble mean values with the standard deviation representing uncertainty (Methods). Subtracting the total PFSC in each simulation from the pre-PETM simulation (exp. 2) provides an estimate of carbon release (right hand column) through the warming sequence in Fig. 2. Bold font has same meaning as in Table 1.

reservoir at the onset of each hyperthermal, extreme warmth and high precipitation rates would have increased silicate weathering, contributing to some $CO_2$ drawdown within the first few $10^3$–$10^4$ years of the event. Once initial cooling and attenuation of orbital variability allowed permafrost to become re-established at high elevations, increasing PFSC sequestration would have accelerated $CO_2$ drawdown despite the diminishing effectiveness of silicate weathering in a cooling climate[29]. On the basis of Holocene rates of PFSC sequestration[22], this mechanism can account for the rapid ($10^4$-year) recovery from the hyperthermals evidenced in carbon isotope records, which has been difficult to explain through silicate weathering alone[9]. The diminishing magnitude of successive Eocene hyperthermals superposed on a backdrop of long-term warming is also explained, given progressively smaller available carbon inventories (Table 1) as permafrost became increasingly restricted to higher elevations.

## METHODS SUMMARY

Model simulations use an updated version of the GENESIS v. 3.0 GCM interactively coupled to the BIOME4 equilibrium vegetation model. The atmospheric component is coupled to surface models including a 50-m slab ocean model with predicted sea surface temperatures, diffusive heat transport, and dynamic-thermodynamic sea ice. Terrestrial land surface components include multi-layer snow and soil models and potential Eocene vegetation distributions are predicted. Model details, early Eocene boundary conditions, validation, and aspects of the soil component relevant to permafrost are discussed in Methods and Supplementary Information. A suite of Palaeocene–Eocene simulations (Table 1) was run with progressively increasing levels of $CO_2$, $CH_4$ and $N_2O$ volume mixing ratios[8], and a range of orbital configurations, including high-eccentricity and high-obliquity orbits corresponding to the onset of hyperthermals (Fig. 1).

PFSC calculations (Table 2) divide permafrost carbon into peatland, near surface, and deep pools such that PFSC $= A_{tot} R \rho D$, where $A_{tot}$ is the permafrost area from each simulation, $R$ is the area ratio, $\rho$ is permafrost carbon density, and $D$ is the thickness of the PFSC deposit. Values of $R$, $\rho$ and $D$ for peatland, near surface, and deep pools are based on theoretical constraints[30] and the modern PFSC inventory[22], resulting in a 12-member ensemble. The ensemble mean is our best estimate of frozen PFSC and the standard deviation represents uncertainty. Values of $R$, $\rho$ and $D$ are described in Methods and Supplementary Information. Carbon releases (Table 2) assume that experiment 2 represents pre-PETM conditions.

**Full Methods** and any associated references are available in the online version of the paper.

1. Nicolo, M. J., Dickens, G. R., Hollis, C. J. & Zachos, J. Multiple early Eocene hyperthermals: their sedimentary expression on the New Zealand continental margin and in the deep sea. *Geology* **35,** 699–702 (2007).
2. Zachos, J. C. *et al.* Rapid acidification of the ocean during the Paleocene–Eocene Thermal Maximum. *Science* **308,** 1611–1615 (2005).
3. Sluijs, A. *et al.* Subtropical Arctic Ocean temperatures during the Palaeocene/Eocene thermal maximum. *Nature* **441,** 610–613 (2006).
4. Higgins, J. A. & Schrag, D. Beyond methane: towards a theory for the Paleocene-Eocene Thermal Maximum. *Earth Planet. Sci. Lett.* **245,** 523–537 (2006).
5. Kurtz, A. C., Kump, L. R., Arthur, M. A., Zachos, J. C. & Paytan, A. Early Cenozoic decoupling of the global carbon and sulfur cycles. *Paleoceanography* **18,** 1090, http://dx.doi.org/10.1029/2003PA000908 (2003).
6. Dickens, G. R., O'Neil, J. R., Rea, D. K. & Owen, R. M. Dissociation of oceanic methane hydrate as a cause of the carbon isotope excursion at the end of the Palaeocene. *Paleoceanography* **10,** 965–971 (1995).
7. Galeotti, S. *et al.* Orbital chronology of Early Eocene hyperthermals from the Contessa Road section, central Italy. *Earth Planet. Sci. Lett.* **290,** 192–200 (2010).
8. Beerling, D. J., Fox, A., Stevenson, D. S. & Valdes, P. J. Enhanced chemistry-climate feedbacks in past greenhouse worlds. *Proc. Natl Acad. Sci. USA* **108,** 9770–9775 (2011).
9. Bowen, G. J. & Zachos, J. Rapid carbon sequestration at the termination of the Palaeocene–Eocene Thermal Maximum. *Nature Geosci.* **3,** 866–869 (2010).
10. Dickens, J. Rethinking the global carbon cycle with a large, dynamic and microbially mediated gas hydrate capacitor. *Earth Planet. Sci. Lett.* **213,** 169–183 (2003).
11. Zeebe, R. E., Zachos, J. & Dickens, G. R. Carbon dioxide forcing alone insufficient to explain Palaeocene-Eocene Thermal Maximum warming. *Nature Geosci.* **2,** 576–580 (2009).
12. Panchuk, K., Ridgwell, A. & Kump, L. R. Sedimentary response to Paleocene-Eocene Thermal Maximum carbon release: a model-data comparison. *Geology* **36,** 315–318 (2008).
13. Buffett, B. & Archer, D. Global inventory of methane clathrate: sensitivity to changes in the deep ocean. *Earth Planet. Sci. Lett.* **227,** 185–199 (2004).
14. Kent, D. V. *et al.* A case for a comet impact trigger for the Paleocene/Eocene thermal maximum and carbon isotope excursion. *Earth Planet. Sci. Lett.* **211,** 13–26 (2003).
15. Storey, M., Duncan, R. A. & Swisher, C. C. III. Paleocene-Eocene Thermal Maximum and the opening of the northeast Atlantic. *Science* **316,** 587–589 (2007).
16. Cramer, B. S., Wright, J. D., Kent, D. V. & Aubry, M.-P. Orbital climate forcing of δ¹³C excursions in the late Paleocene–early Eocene (chrons C24n-C25n). *Paleoceanography* **18,** 1097, http://dx.doi.org/10.1029/2003PA000909 (2003).
17. Lourens, L. *et al.* Astronomical pacing of late Palaeocene to early Eocene hyperthermal events. *Nature* **435,** 1083–1087 (2005).
18. Laskar, J. *et al.* A long-term numerical solution for the insolation quantities of the Earth. *Astron. Astrophys.* **428,** 261–285 (2004).
19. Westerhold, T., Röhl, U., McCarren, H. K. & Zachos, J. C. Latest on the absolute age of the Paleocene–Eocene Thermal Maximum (PETM): new insights from exact stratigraphic position of key ash layers +19 and −17. *Earth Planet. Sci. Lett.* **287,** 412–419 (2009).
20. Schuur, E. A. G. *et al.* Vulnerability of permafrost carbon to climate change: implications for the global carbon cycle. *Bioscience* **58,** 701–714 (2008).
21. Wilson, D. S. & Luyendyk, B. P. West Antarctic paleotopography estimated at the Eocene-Oligocene climate transition. *Geophys. Res. Lett.* **36,** L16302 (2009).
22. Tarnocai, C. *et al.* Soil organic carbon pools in the northern circumpolar permafrost region. *Glob. Biogeochem. Cycles* **23,** GB2023, http://dx.doi.org/10.1029/2008GB003327 (2009).
23. Ronov, A., Khain, V. & Balukhovsky, S. *Atlas of Lithological-Paleogeographical Maps of the World: Mesozoic and Cenozoic of Continents and Oceans* (eds Barsukov, V. L. & Laviorov, N. P.) (Moscow Editorial Publishing Group VNII Zarubezh-Geologia, Moscow, 1989).
24. Sloan, L. C., Walker, J. C. G., Moore, T. C. Jr & Rea, D. K. Possible methane-induced polar warming in the early Eocene. *Nature* **357,** 320–322 (1992).
25. Kalkreuth, W. D. *et al.* Petrological, palynological and geochemical characteristics of Eureka Sound group coals (Stenkul Fiord, southern Ellesmere Island, Arctic Canada). *Int. J. Coal Geol.* **30,** 151–182 (1996).
26. Röhl, U., Brinkhuis, H., Sluijs, A. & Fuller, M. in *The Cenozoic Southern Ocean: Tectonics, Sedimentation, and Climate Change between Australia and Antarctica* (eds Exon, N. F., Malone, M. & Kennett, J. P.) 113–125 (Geophysical Monograph Series 151, American Geophysical Union, 2004).
27. Schaefer, K., Zhang, T., Bruhwiler, L. & Barrett, A. P. Amount and timing of permafrost carbon release in response to climate warming. *Tellus B* **63,** 165–180 (2011).
28. Elberling, B., Christensen, H. H. & Hansen, B. U. High nitrous oxide production from thawing permafrost. *Nature Geosci.* **3,** 332–335 (2010).
29. Pagani, M., Caldeira, K., Berner, R. & Beerling, D. The role of terrestrial plants in limiting atmospheric $CO_2$ decline over the past 24 million years. *Nature* **460,** 85–88 (2009).
30. Clymo, R. S. The limits to peat bog growth. *Phil. Trans. R. Soc. Lond. B* **303,** 605–654 (1984).
31. Zachos, J. C., Dickens, G. R. & Zeebe, R. E. An early Cenozoic perspective on greenhouse warming and carbon-cycle dynamics. *Nature* **451,** 279–283 (2008).

## METHODS

**Climate–vegetation–soil model.** The current (2011) version of the GENESIS v. 3.0 GCM[32] is interactively coupled to the BIOME4 equilibrium vegetation model[33]. The model has been tested extensively in present day and palaeoclimate scenarios and produces distributions of potential vegetation and permafrost close to observations. The atmospheric component has 18 vertical layers, a spectral resolution of T31 (~3.75°), and uses an adapted version of the NCAR CCM3 solar and thermal infrared radiation code[34]. The model atmosphere is coupled to $2° \times 2°$ surface models including a 50-m slab ocean model with prognostic sea surface temperatures, diffusive heat transport, and dynamic-thermodynamic sea ice. Terrestrial land surface components include multi-layer snow and soil models, and a land-surface-transfer scheme (LSX) that calculates momentum transfer and fluxes of energy and water between the atmosphere and ice, snow, soil surfaces, and upper and lower vegetation canopies. This version of the GCM has a sensitivity to $2 \times CO_2$ of 2.9 °C, without vegetation, GHG, or ice sheet feedbacks.

In the absence of Eocene vegetation data with global coverage, potential equilibrium vegetation distributions are predicted by BIOME4. The model predicts the distribution, community structure and biogeochemistry of 27 biomes using monthly climatologies of temperature, precipitation and clouds simulated by the GCM. In turn, the simulated vegetation provides the physical land-surface attributes in the GCM. Climate-biome simulations (Table 1) were run for 40 years to allow equilibration and climatological means were calculated from the last 10 years.

The soil model[35] has six layers with the bottom of each layer 0.5, 0.15, 0.25, 0.75, 1.75 and 4.25 m below the surface. The model predicts evolving vertical profiles of temperature, moisture and frozen water in response to the surface climatology, snow cover, soil hydraulic properties, drainage through the bottom of the soil column, and coupling between frozen pore space and hydraulics. Given the spatial resolution of our model ($2° \times 2°$) and unresolved details of Eocene topography, we estimate total permafrost region (Table 1) rather than the smaller (sub-grid scale) area of actual frozen ground. In our modern control simulation, this produces a permafrost distribution and area ($23.3 \times 10^6$ km$^2$) very close to observations ($22.8 \times 10^6$ km$^2$)[36]. In our warm Eocene simulations, perennially frozen ground is mostly limited to layers 5 and 6, with an extensive active layer above. Calculated permafrost areas are based on layer 6.

**Model boundary conditions and inputs.** Model boundary conditions include a new hybrid reconstruction of early Eocene global geography, with Antarctic shorelines and elevations in a prior reconstruction[37] replaced with the new (larger) Antarctic reconstruction[21] (Supplementary Information). A suite of simulations (Table 1) was run with progressively increasing levels of GHGs, assuming background levels increased steadily from the Palaeocene until the Early Eocene Climatic Optimum (~51 Myr ago), with punctuated, transient increases at the hyperthermals[8,11,38]. Prescribed $CO_2$, $CH_4$ and $N_2O$ atmospheric mixing ratios are based on a combination of proxy estimates of $CO_2$ and estimates of $CH_4$ and $N_2O$ simulated using a three-dimensional Earth system model incorporating chemistry–climate feedbacks[8]. Excluding the hyperthermals, background levels of late Palaeocene–early Eocene atmospheric $CO_2$ are assumed to range from 500 p.p.m.v. to 1,000 p.p.m.v. (refs 11, 38), with atmospheric $CH_4$ increasing from 1,200 p.p.b.v. to 3,000 p.p.b.v. and $N_2O$ increasing from 350 p.p.b.v. to 400 p.p.b.v. in response to an enhanced hydrological cycle and expanded wetlands on a mostly ice-free world[8]. For comparative purposes, the combined radiative forcing potential of prescribed $CO_2$, $CH_4$ and $N_2O$ are converted to equivalent $CO_2$ volume mixing ratios (e.p.p.m.v.) using standard expressions[39,40].

Prescribed orbital configurations (Table 1) use values for eccentricity and obliquity chosen to broadly represent those occurring during high-eccentricity and high-obliquity orbital nodes. The orbital parameters do not attempt to represent specific time slices, which are uncertain in orbital solutions of Eocene age[18].

**Permafrost-soil organic carbon calculations.** Lacking observations of Palaeogene permafrost distribution, carbon content and topography, we estimate frozen permafrost soil carbon (PFSC) using current observations, assuming past permafrost conditions are similar to today, differing only in the total permafrost area. We divide frozen PFSC into peatland, near surface and deep pools such that:

$$PFSC = A_{tot}R\rho D \qquad (1)$$

where $A_{tot}$ is the total permafrost area from each simulation, $R$ is the ratio of pool area to total permafrost area, $\rho$ is the permafrost carbon density, and $D$ is the thickness of the PFSC deposit. Peatland $R$ is the ratio of modern wetland area to total permafrost area[22] and near surface $R$ is one minus peatland $R$. An analysis of the reconstructed topography (Supplementary Information) indicates that ~15–30% of the permafrost land area has surface slopes ($<0.1\%$) suitable for the development of peatland, consistent with modern wetland area fraction for permafrost regions. The value for peatland $R$ is conservative, considering that

estimates of Palaeocene–Eocene wetland area are up to 3 times greater than today[8,23,24,41]. Deep PFSC deposits form under special conditions of especially fast sedimentation: deltaic deposits and the aeolian deposition that formed the modern yedoma deposits. $R$ for deep deposits is the ratio of areas with known deep deposits to total permafrost area[22]. The near surface and deep deposits have a $\rho$ of either 21 or 30 kg m$^{-3}$ based on typical observed values[22,42–44] and peatland $\rho$ is based on observed peat densities[45]. $D$ for near-surface PFSC deposits is either the thickness of the lowest layer of the model (2.5 m) or the average simulated permafrost thickness, $D_{ave}$. $D_{ave}$ is the maximum depth of the soil column (4.25 m) minus the average active layer thickness defined by the zero degree isotherm. $D_{ave}$ ranges between 2.4 and 3.1 m with an average of 2.6 m. For the modern control run, we accounted for the much shorter accumulation times by setting a maximum PFSC depth of 3 m, resulting in a $D$ of 1.4 m. $D$ for deep deposits is 22 m (ref. 22).

The peatland $D$ assumes mature, steady state peat development. A peat bog consists of upper acrotelm and lower catotelm layers, divided by the depth of the summer water table[30]. The frozen PFSC is located in the catotelm below the water table. Peatland $D$ is the thickness of the catotelm, which is a balance of organic matter settling out of the acrotelm and loss of matter due to decay[30]:

$$\frac{\partial D}{\partial t} = \frac{p_c}{\rho} - \frac{D}{\tau} \qquad (2)$$

where $p_c$ is the flux of carbon from the acrotelm (kg m$^{-2}$ yr$^{-1}$), and $\tau$ is the catotelm decay rate (yr). After ~50,000 years, input balances decay and $D$ approaches a constant, steady state value[30]. Continuous deposition on unglaciated terrain before the PETM and between most hyperthermals lasted $>10^6$ years, so on average, peatlands were near steady state. Setting the time derivative to zero and rearranging gives:

$$D = \frac{p_c \tau}{\rho} \qquad (3)$$

We assume a $\tau$ of 15,000 years and a $p_c$ of $0.027 \pm 0.019$ kg m$^{-2}$ yr$^{-1}$ based on typical observed values[30] to estimate a peatland $D$ of $2.9 \pm 2.0$ m.

Values of $R$, $\rho$ and $D$ used for peatland, near-surface, and deep PFSC deposits (Supplementary Information) provide an ensemble of 12 members. The ensemble mean is our best estimate of frozen PFSC and the standard deviation is uncertainty. Subtracting PFSC from the pre-PETM simulation (experiment 2) gives the potential release for each simulation. The effect of PFSC release on atmospheric $CO_2$, ignoring other feedbacks, assumes a relationship of 0.4602 p.p.m.v. per Pg C (ref. 27). A rate of carbon release up to 1.5 Pg C yr$^{-1}$ (Supplementary Information) is derived by scaling to model calculations of future permafrost[27] and modern observations[46]. Carbon isotopic values are expressed as $[R(\text{sample})/R(\text{standard}) - 1] \times 1,000$, where $R$ is the $^{13}C/^{12}C$ ratio of sample relative to the Peedee Belemnite standard.

32. Thompson, S. L. & Pollard, D. Greenland and Antarctic mass balances for present and doubled atmospheric $CO_2$ from the GENESIS Version-2 Global Climate Model. *J. Clim.* **10,** 871–900 (1997).
33. Kaplan, J. O. *et al.* Climate change and Arctic ecosystems: 2. Modeling, paleodata-model comparisons, and future projections. *J. Geophys. Res.* **108** (D19), 8171, http://dx.doi.org/10.1029/2002JD002559 (2003).
34. Kiehl, J. T. *et al.* The National Center for Atmospheric Research Community Climate Model: CCM3. *J. Clim.* **11,** 1131–1149 (1998).
35. Thompson, S. L. & Pollard, D. A global climate model (GENESIS) with a land-surface-transfer scheme (LSX). Part I: present-day climate. *J. Clim.* **8,** 732–761 (1995).
36. Zhang, T., Heginbottom, J. A., Barry, R. G. & Brown, J. Further statistics on the distribution of permafrost and ground ice in the northern hemisphere. *Polar Geogr.* **24,** 126–131 (2000).
37. Sewall, J. O., Sloan, L. C., Huber, M. & Wing, S. Climate sensitivity to changes in land surface characteristics. *Glob. Planet. Change* **26,** 445–465 (2000).
38. Pagani, M., Caldeira, K., Archer, D. E. & Zachos, J. An ancient carbon mystery. *Science* **314,** 1556–1557 (2006).
39. Ramaswamy, V. *et al.* in *Climate Change 2001: The Scientific Basis* (eds Haughton, J. T. *et al.*) 351–416 (Cambridge Univ. Press, 2001).
40. Shi, G. Radiative forcing and greenhouse effect due to the atmospheric trace gasses. *Sci. China B* **35,** 217–229 (1992).
41. Beerling, D., Berner, R. A., Mackenzie, F. T., Harfoot, M. B. & Pyle, J. A. Methane and the $CH_4$-related greenhouse effect over the past 400 million years. *Am. J. Sci.* **309,** 97–113 (2009).
42. Dutta, K., Schuur, E. A. G., Neff, J. C. & Zimov, S. A. Potential carbon release from permafrost soils of Northeastern Siberia. *Glob. Change Biol.* **12,** 2336–2351 (2006).
43. Khvorostyanov, D. V., Ciais, P., Krinner, G. & Zimov, S. A. Vulnerability of east Siberia's frozen carbon stores to future warming. *Geophys. Res. Lett.* **35,** L10703, http://dx.doi.org/10.1029/2008GL033639 (2008).
44. Zech, M. *et al.* Characterization and palaeoclimate of a loess-like permafrost palaeosol sequence in NE Siberia. *Geoderma* **143,** 281–295 (2008).
45. Price, J. S., Cagampan, J. & Kellner, E. Assessment of peat compressibility: is there an easy way? *Hydrol. Process.* **19,** 3469–3475 (2005).
46. Schuur, E. A. G. *et al.* The effect of permafrost thaw on old carbon release and net carbon exchange from tundra. *Nature* **459,** 556–559 (2009).

# CORRECTIONS & AMENDMENTS

## Corrigendum: Past extreme warming events linked to massive carbon release from thawing permafrost

Robert M. DeConto, Simone Galeotti, Mark Pagani,
David Tracy, Kevin Schaefer, Tingjun Zhang, David Pollard
& David J. Beerling

In the online-only Methods of our Letter, several erroneous values appear among the parameters used to calculate peatland $D$, the average thickness of permafrost peatland deposits. Catotelm decay rate ($\tau$) used in our equation 3 was incorrectly listed as 1,500 years instead of 15,000 years. $p_c$, the carbon flux from the acrotelm into the catotelm ($kg\,m^{-2}\,yr^{-1}$), appeared as $0.27 \pm 0.19\,kg\,m^{-2}\,yr^{-1}$ instead of $0.027 \pm 0.019\,kg\,m^{-2}\,yr^{-1}$. Using the correct values has no effect on the calculation of peatland $D$, because the decimal point errors cancel in equation 3. In addition, peat carbon density ($\rho$) listed in Supplementary Table 1 was incorrect and shown as peat density instead of peat carbon density. Using the correct value for $\rho$ in equation 3 doubles the estimated average thickness of permafrost peat deposits $D$, but does not change the calculated carbon inventories discussed in the text or in Table 2. These errors do not affect the conclusions of the Letter. All values of model parameters used in equation 3 have been corrected in the HTML and PDF versions online. The Supplementary Information has been corrected online. We thank C. J. Williams for pointing out the decimal point error associated with $p_c$ and S. Frolking for noting the cancelling decimal point errors associated with $p_c$ and $\tau$, and the erroneous value of peat carbon density ($\rho$) and its effect on peatland $D$.